A 3D pencil-beam-based superposition algorithm for photon dose calculation in heterogeneous media

L Tillikainen[1], **H Helminen**[1,3], **T Torsti**[1], **S Siljamäki**[1], **J Alakuijala**[1,3], **J Pyyry**[1] and **W Ulmer**[2]

[1] Varian Medical Systems Finland Oy, Paciuksenkatu 21, FIN-00270 Helsinki, Finland
[2] Varian Medical Systems Imaging Laboratory GmbH, Täfernstrasse 7, CH-5405 Baden-Dättwil, Switzerland

E-mail: laura.tillikainen@varian.com

Abstract

In this work, a novel three-dimensional superposition algorithm for photon dose calculation is presented. The dose calculation is performed as a superposition of pencil beams, which are modified based on tissue electron densities. The pencil beams have been derived from Monte Carlo simulations, and are separated into lateral and depth-directed components. The lateral component is modeled using exponential functions, which allows accurate modeling of lateral scatter in heterogeneous tissues. The depth-directed component represents the total energy deposited on each plane, which is spread out using the lateral scatter functions. Finally, convolution in the depth direction is applied to account for tissue interface effects. The method can be used with the previously introduced multiple-source model for clinical settings. The method was compared against Monte Carlo simulations in several phantoms including lung- and bone-type heterogeneities. Comparisons were made for several field sizes for 6 and 18 MV energies. The deviations were generally within (2%, 2 mm) of the field central axis d_{max}. Significantly larger deviations (up to 8%) were found only for the smallest field in the lung slab phantom for 18 MV. The presented method was found to be accurate in a wide range of conditions making it suitable for clinical planning purposes.

1. Introduction

Modeling the dose deposition of a therapeutic photon beam in a patient geometry is an interesting problem, and numerous algorithms have been proposed for this purpose. Monte Carlo methods have become available for clinical treatment planning due to improvements in

---

[3] Present address: Google, Freigutstrasse 12, CH-8002, Zürich, Switzerland.

computation power, transport algorithms and variance reduction techniques (Neuenschwander *et al* 1995, Ma *et al* 1999, Kawrakow 2000, Kawrakow and Fippel 2000). Monte Carlo methods can be very accurate especially in complex treatment geometries and in the presence of tissue heterogeneities, but can still be too slow for routine clinical use, especially if high statistical accuracy is required. Another accurate approach is to solve the coupled photon and electron transport equations directly in the patient geometry using the finite-element multigroup discrete ordinates method (Gifford *et al* 2006, Wareing *et al* 2007). This method, however, is presently not available for clinical use.

Other modeling techniques rely on more macroscopic characterizations of therapeutic radiation beams via the use of radiation kernels (convolution/superposition methods). Typically, the kernel superposition methods are based either on pencil beams or on point-spread functions. In pencil-beam superposition, the kernel represents the dose contribution of a very narrow beam, and the kernels are modulated by the incoming photon fluence to produce the final dose distribution (Boyer and Mok 1986, Storchi *et al* 1999, Ulmer *et al* 2005). In point-spread function superposition, the kernel consists of the dose deposited by photons whose first interaction is forced to a single point in the phantom. In order to obtain the dose distribution, the point-spread functions are modulated by the total energy released per unit mass (TERMA) distribution (Mackie *et al* 1985, Sharpe and Battista 1993, Miften *et al* 2000).

In this work, we present a 3D pencil-beam kernel-based superposition algorithm, which is a continuation of earlier work by our research group (Ulmer *et al* 2005). Compared to the prior work, exponential functions are now used instead of Gaussian functions to model lateral phantom scatter. This allows for more accurate modeling of the scatter near borders of lateral heterogeneities. Furthermore, the modeling of electron transport has been revised. Instead of the earlier method, which was based on the modeling of local electron disequilibrium with forward and backward electron kernels, build-up is now modeled with a conceptually simpler convolution kernel model. The resulting algorithm is efficient, and yet produces dose distributions that are comparable to point-spread-function-based algorithms, such as the collapsed cone convolution (CCC) model—see section 3 and the results presented by Arnfield *et al* (2000). The method has been commercially released as the Anisotropic Analytical Algorithm (AAA), which has been integrated into the Eclipse^{TM} Integrated Treatment Planning System (Varian Medical Systems Inc., Palo Alto, CA).

This paper describes the methods and principles used in the design of the algorithm, and gives a detailed and complete description of the theory and assumptions therein. Especially the heterogeneity correction method, and the build-up and build-down corrections are discussed in detail. Earlier articles of the current algorithm have focused on the validation results in clinical settings (Fogliata *et al* 2006, Van Esch *et al* 2006) and on the source model and its adaptation to an individual treatment unit (Tillikainen *et al* 2007). In this work, the dose calculations using the presented method are compared to Monte Carlo simulations in phantom geometries that are representative of realistic situations. Previously, the comparisons have been performed mostly against experimental measurements, which can sometimes be difficult to conduct and interpret—especially in heterogeneous phantoms.

2. Methods and materials

First, we discuss the methods and principles used when designing the algorithm. Then we derive the method of reconstructing pencil beams from lateral and depth-directed components. Finally, we discuss the necessity of a short-range energy transfer to account for build-up and build-down effects near the boundaries of tissue heterogeneities.

2.1. Source model

Accurate characterization of therapeutic photon beams requires the modeling of different radiation sources in the linear accelerator. Here we use a multiple-source model developed by the authors (Tillikainen *et al* 2007). The source model for the open beam consists of a primary photon source for bremsstrahlung radiation from the target, an extra-focal distributed source accounting for photons scattered in the accelerator head and an electron contamination source. The method presented in this work is used to calculate the dose distribution resulting from all of the components mentioned above. However, the pencil-beam model is best adapted to a situation where all particles originate from a single point-like source, and hence the presentation focuses on the primary photon component.

The spectrum and energy fluence of the primary photon radiation vary across the beam, mainly due to the initial angular distribution of the bremsstrahlung photons and the uneven attenuation of photons in the flattening filter. The spatially varying primary energy fluence is denoted by $\Phi_{\mathrm{prim}}(\boldsymbol{r})$, where $\boldsymbol{r}$ is a point on the reference plane. Similarly, the energy fluences from the extra-focal photon and electron contamination sources are denoted by $\Phi_{\mathrm{ef}}(\boldsymbol{r})$ and $\Phi_{\mathrm{el}}(\boldsymbol{r})$, respectively. The model presented here is able to account for spectral variations across the broad beam. We have found that it is crucial for the accurate modeling of the beam shape and penumbra for various field sizes.

2.2. Diverging coordinate system

The use of a diverging coordinate system is beneficial for manipulating the pencil beams when the radiation can be assumed to originate from a single point, the target, which is chosen as the origin $\mathbf{o}$. We have chosen an orthonormal base such that the positive z-axis passes through the isocenter $(0, 0, d_{\mathrm{SAD}})$, where d_{SAD} is the distance from the target to the isocenter, and x- and y-axes are aligned with the respective collimator axes. Then a diverging mapping $\mathcal{M}: \mathbb{R}^3_+ \mapsto \mathbb{R}^3_+$ is defined in the following way:

$$\boldsymbol{x} \mapsto \left(\frac{d_{\mathrm{SAD}}}{x_z} x_x, \frac{d_{\mathrm{SAD}}}{x_z} x_y, \sqrt{x_x^2 + x_y^2 + x_z^2} \right) := \boldsymbol{p}, \tag{1}$$

where $\mathbb{R}^3_+$ is the half-space of $\mathbb{R}^3$ with $z > 0$, $\boldsymbol{x} = (x_x, x_y, x_z)$ is a vector in the orthogonal coordinate system and $\boldsymbol{p} = (p_x, p_y, p_z)$ is a vector in the diverging coordinate system. It is evident that $\mathcal{M}$ maps point on lines that pass through $\mathbf{o}$ to lines of constants p_x and p_y. Similarly, spherical shells are mapped to constant p_z. While this is not the only possible choice for a diverging mapping, the use of spherical shells makes it easier to avoid bias caused by oblique kernels, and the definitions of p_x and p_y have an intuitive meaning as projections onto the isocenter plane. In the computer implementation of the method, the discrete points in the diverging coordinate system are chosen such that the distance between neighboring points in the grid is equal to Δ, which is a run-time parameter of the algorithm. The incoming energy fluence $\Phi_{\mathrm{prim}}(\boldsymbol{r})$ is also discretized into cones, whose intersection with the isocenter plane is a square with side length Δ, and the center of the square aligns with the grid points. Thus, it is assumed that the radiation intensity is constant within the area of each cone or beamlet.

2.3. Monte-Carlo-derived pencil-beam kernels

We denote the pencil-beam kernel function produced by a narrow beam of monoenergetic photons of energy E, impinging on a semi-infinite perpendicular water phantom, as $h_E(z, r)$. Here z and r represent the distance from the surface and the orthogonal distance from the central axis, respectively. The kernels $h_E(z, r)$ have been obtained from Monte Carlo simulations

using the DOSRZnrc user code of EGSnrc (Kawrakow 2000). Each monoenergetic kernel h_E has been simulated using ten million particle histories, which results in a statistical standard uncertainty of about 0.3% in the peak dose region for all energies. However, the exact statistical standard uncertainty varies slightly for different energies. In order to perform a superposition of the pencil-beam kernels, they must be re-sampled into the diverging coordinate system via the mapping $\mathcal{M}$. It is also necessary to compensate for the oblique incidence of the primary beam with the patient surface.

Given a primary ray β, we first create a poly-energetic pencil-beam kernel $h_{\beta,\mathrm{cyl}}$ as a superposition of mono-energetic kernels h_E weighted by the spectrum $S_\beta(E)$ of beamlet β:

$$h_{\beta,\mathrm{cyl}}(z, r) = \frac{\int h_E(z, r) S_\beta(E)\,\mathrm{d}E}{\int S_\beta(E)\,\mathrm{d}E}, \tag{2}$$

where the subscript 'cyl' denotes the cylindrical coordinate system in which the kernel is defined. It would be possible to directly map $h_{\beta,\mathrm{cyl}}(z, r)$ into the diverging coordinate system using $\mathcal{M}$, and determine the position within the pencil beam with an offset from the origin, but this would introduce bias since area and distance are not invariant on translation in $\mathcal{M}$. The correct way is to first align the pencil beam $h_{\beta,\mathrm{cyl}}$ with the ray β using an orthogonal rotation and translation $\mathcal{R}_\beta$ and then use the inverse mapping $\mathcal{M}^{-1}$ to find the corresponding position in the orthogonal coordinate system. Hence, the pencil beam for beamlet β in the diverging coordinate system is defined as

$$h_\beta(\boldsymbol{p}) = h_{\beta,\mathrm{cyl}}\big(\mathcal{R}_\beta^{-1}(\mathcal{M}^{-1}(\boldsymbol{p}))\big)|\det(J(\mathcal{M}))|, \tag{3}$$

where J is the Jacobian of mapping $\mathcal{M}$ evaluated at $\boldsymbol{p}$; the absolute value of the determinant accounts for non-uniform volume mapping of the $\mathcal{M}$ operator. $\mathcal{M}^{-1}(\boldsymbol{p})$ maps the point $\boldsymbol{p}$ from a diverging to a cylindrical coordinate system and $\mathcal{R}_\beta^{-1}$ rotates and translates the point back such that the beamlet is aligned along the field central axis (CAX). It should be noted that the resulting kernel $h_\beta(\boldsymbol{p})$ does not have cylindrical symmetry in the diverging coordinates, and hence is subscripted with three coordinates $\boldsymbol{p} = (p_x, p_y, p_z)$.

2.4. Exponential modeling of pencil beams

The method described here assumes that the pencil beam can be separated into depth-directed and lateral components. The depth-directed component accounts for the total energy deposited by the pencil beam for each layer p_z in the calculation grid (Ulmer *et al* 2005):

$$I_\beta(p_z) = \Phi_\beta \iint h_\beta(t, \upsilon, p_z)\,\mathrm{d}t\,\mathrm{d}\upsilon, \tag{4}$$

where Φ_β is the primary energy fluence for the beamlet β.

Lateral dose deposition is modeled as a sum of N radial exponential functions. Due to lack of cylindrical symmetry, the modeling is slightly different for each angle θ around the central axis of the beamlet β. For each depth p_z and angle θ, we denote with $f_\beta(\theta, \lambda, p_z)$ the fraction of energy deposited onto an infinitesimally small angular sector at distance λ from the beamlet central axis. The division into angular sectors is necessary, since the heterogeneity correction in the lateral direction is performed by ray tracing along the discrete rays that represent the collapsed sectors, as we shall later present. f_β is calculated in the following way from the Monte-Carlo-derived data:

$$f_\beta(\theta, \lambda, p_z) = \lambda h_\beta(p_x + \lambda \cos\theta, p_y + \lambda \sin\theta, p_z)/I_\beta(p_z), \tag{5}$$

where (p_x, p_y, p_z) are the coordinates of a point $\boldsymbol{p}$ within the beamlet β. The division with $I_\beta(p_z)$ is required to normalize the integral of f_β to unity over each calculation plane.

Given a set of N attenuation coefficients μ_i, the exponential representation of the lateral pencil-beam component is of the form

$$k_\beta(\theta, \lambda, p_z) = \sum_{i=1}^{N} c_i(\theta, p_z) \frac{1}{\mu_i} e^{-\mu_i \lambda}, \tag{6}$$

where the attenuation coefficients μ_i are the same for all planes to allow efficient computer implementation. The weight parameters $c_i(\theta, p_z)$ are chosen such that the error between f_β and k_β is minimized, when they are viewed as functions of λ. The parameter N offers a speed-quality parameter in the computer implementation of this method: the value $N = 6$ has been used throughout this work. The μ_i parameters have been chosen such that the effective ranges $1/\mu_i$ vary from 1 mm to 200 mm with equal logarithmic intervals.

Accurate fitting between Monte-Carlo-simulated data and the parameterized model is important to be able to create a model that can be used over a wide range of field sizes and beam modulation techniques. We have used a linear least squares fitting of the following integral functions:

$$F_\beta(\theta, \lambda, p_z) = \int_{t=0}^{\lambda} f_\beta(\theta, t, p_z) \, dt, \tag{7}$$

$$K_\beta(\theta, \lambda, p_z) = \int_{t=0}^{\lambda} k_\beta(\theta, t, p_z) \, dt. \tag{8}$$

Thus, the fitting is essentially performed by first multiplying the kernels with the radius λ in (5) and then performing the integral transform in (7) and (8). To see why these steps are important, it should be noted that the component values with larger radius are deposited over larger areas, so multiplication by radius accounts for this increased weight. The integral transform, on the other hand, assures that the errors in the linear fitting procedure are more evenly distributed, since it effectively penalizes for consecutive errors of the same sign. The F_β function can also be viewed as a circular phantom scatter factor for a beam with radius λ, if the lack of exact cylindrical symmetry is ignored. This provides intuitive support on the fact that the accurate modeling of F_β is important to account for the small-to-large field size characteristics of the model.

2.5. Superposition of pencil beams

In a homogeneous water-equivalent phantom, the energy $E_\beta(p)$ deposited from a pencil-beam beamlet β into a grid point p is the product of the energy deposited on the calculation plane (I_β) and the corresponding lateral scatter kernel (k_β). A factor of $1/\lambda$ is also included to counter-effect the multiplication with λ performed during the fitting process:

$$E_\beta(p) = I_\beta(p_z) \frac{1}{\lambda} k_\beta(\theta, \lambda, p_z). \tag{9}$$

To account for non-water-equivalent patient tissue, we use the approximation where each spatial dimension of the scatter process is scaled locally by the inverse relative electron density $1/\rho_w$ defined as

$$\rho_w(p) := \rho^{elec}(p) / \rho_{water}^{elec}, \tag{10}$$

where ρ^{elec} is the local electron density at point p and ρ_{water}^{elec} is the electron density of water. This is a common approach when accounting for the tissue heterogeneities in kernel-based models (Ahnesjö and Aspradakis 1999), and has been reported to be more accurate than the scaling based on mass density (Seco and Evans 2006). If we assume that this approximation

holds, one still has to take into account the fact that the scattered particles follow different paths through the medium. In kernel-superposition-based methods, this is often done by combining all the possible paths into fewer collapsed paths and using the assumption that the effects of heterogeneity can be corrected along these paths. In the method presented here, this is done by assuming that the I function and origin-centered rays of the k functions can be independently scaled. This corresponds to paths, where particles are first assumed to arrive at the destination spherical shell p_z via the centerline of the beamlet and then travel to the destination voxel along the spherical shell. While this is clearly an approximation, it should be noted that it only affects the heterogeneity correction. In water, this procedure essentially corresponds to a lookup from the Monte-Carlo-derived kernel, which produces no additional errors (assuming that the errors introduced in the fitting of the exponential functions to Monte-Carlo-derived data are negligible).

To scale the function I, it is thus necessary to account for the effective (radiological) distance between the pencil-beam entry point and the calculation plane computed as $d_{\text{eff}}(X) = \int_X \rho_{\text{w}}(\boldsymbol{p}) \, \mathrm{d}\boldsymbol{p}$ for an arbitrary curve X. When the I function is expressed in terms of true depth p_z instead of effective depth p_z', it is also necessary to scale by the local electron density due to the change of variables. Thus, the heterogeneity-corrected depth-directed component I_β' is calculated as

$$I_\beta'(p_z) = I_\beta(p_z')\rho_{\text{w}}(\boldsymbol{p}_\beta), \tag{11}$$

where $\boldsymbol{p}_\beta$ is the point on the pencil-beam central axis at depth p_z and p_z' is the effective depth given by $d_{\text{eff}}(P_\beta)$, where P_β is the path from the pencil-beam entry point to $\boldsymbol{p}_\beta$.

The scaling of the lateral scatter kernel is done in a similar fashion, calculating the radiological path length in a radial manner from the center of the pencil beam. Specifically for point $\boldsymbol{p}$, we assume that $C_\beta(\theta, p_z)$ is the curve following $\{\mathcal{M}^{-1}(t\boldsymbol{p}_\beta + (1-t)\boldsymbol{p})\}$, where $0 \leqslant t \leqslant 1$. Then the heterogeneity-corrected lateral kernel $k_\beta'(\theta, \lambda, p_z)$ is given by

$$k_\beta'(\theta, \lambda, p_z) = k_\beta\left(\theta, \frac{p_z'}{p_z}\lambda', p_z'\right)\rho_{\text{w}}(\boldsymbol{p}), \tag{12}$$

where λ' is the effective radius computed as $\lambda' = d_{\text{eff}}(C_\beta(\theta, p_z))$. It is necessary to use the lateral scatter kernel from the effective depth p_z', which is why the effective radius is also scaled by the ratio p_z'/p_z that corrects for the diverging coordinate system. An alternative strategy that may lead to more efficient computer implementation is to perform this scaling to the f_β function defined in (5) before the exponential fitting is done, which allows performing the actual deposition using incremental methods.

The heterogeneity-corrected energy distribution from a single beamlet β is then calculated as

$$E_\beta(\boldsymbol{p}) = I_\beta'(p_z)\frac{1}{\lambda}k_\beta'(\theta, \lambda, p_z). \tag{13}$$

In computer implementation, it is necessary to choose a discrete number of angular sectors over which the superposition is performed. We have used $\Delta\theta = \pi/8$ or $\Delta\theta = \pi/4$ corresponding to 16 and 8 discrete superposition directions depending on the effective range $1/\mu_i$ in question. The total energy deposited into a grid point $\boldsymbol{p}$ is then simply an integral of the contributions of the individual beamlets over the broad beam area:

$$E_{\text{tot}}(\boldsymbol{p}) = \iint_{\beta'} E_{\beta'}(\boldsymbol{p}) \, \mathrm{d}\beta'. \tag{14}$$

2.6. Build-up and build-down corrections

The separation of the heterogeneity correction into two components, the depth-directed component in (11) and lateral scatter component in (12), is clearly an approximation, but it has the desirable attribute that the pencil-beam kernel is scaled in all dimensions by the reciprocal of ρ_w when calculating the dose to a uniform phantom with non-water-equivalent electron density ($\rho_w \neq 1$). It also produces results that are equivalent to Monte Carlo simulations after a sufficient distance from the material interface in slab-like phantoms. However, near the interfaces, the method as presented above would fail to reproduce the gradual build-up and build-down effects; instead, the dose would jump abruptly to a new equilibrium level. This is caused by the fact that the scattered particles originating before the interface are not correctly taken into account by this method.

The size of the build-up or build-down transition is determined by the mean range of the scattered particles. Also, the dominant scatter component in a therapeutic radiation beam is forward directed. Thus to reproduce these effects using a pencil-beam-based model, it is not sufficient to scale the pencil beam in its entirety by the effective distance, but a method to account for the forward-directed energy shift is needed.

The technique chosen in this work is to employ a forward build-up convolution kernel to the energy deposition. The build-up kernel k_b is a dual exponential function of the form

$$k_b(d) = \begin{cases} \sum_{i=1}^{2} g_i \dfrac{1}{\nu_i} \, \mathrm{e}^{-\nu_i d}, & \text{when} \quad d \geqslant 0 \\ 0 & \text{otherwise,} \end{cases} \tag{15}$$

where the parameters g_i and ν_i determine the shape of the kernel. Setting $\sum g_i = 1$ guarantees the preservation of energy in the convolution process. The free parameters g_1, ν_1 and ν_2 are chosen such that the build-up effect between vacuum and water is preserved, as explained later in this section.

The convolution is done with the energy density distribution in terms of the effective distance in the following way:

$$E_b(\boldsymbol{p}) = \int_{t=0}^{p_z} E_{\text{tot}}(p_x, p_y, t) k_b(d_{\text{eff}}) \rho_w(p_x, p_y, t) \, \mathrm{d}t, \tag{16}$$

where d_{eff} is the (signed) effective distance from (p_x, p_y, p_z) to (p_x, p_y, t), and the multiplication with ρ_w is due to the change of variables from the effective depth to true depth. This correction effectively shifts energy deeper, so the original pencil beams would no longer be accurately reproduced. For example, the original build-up at the surface of the pencil beam would be further stretched. Hence, it is necessary to pre-compensate for it either in the original Monte Carlo kernel in (2) or in the I function in (4). For simplicity, we have chosen the latter approach. The operation to be performed on the I function is the inverse convolution (deconvolution) with the kernel k_b. Otherwise, the calculation of scatter is done as explained in the previous sections, except that the pre-compensated function I_{pre} is used instead of I in (11). Since deconvolution is an inherently unstable operation, we have used a linear least squares method augmented with the Tikhonov regularization (Tikhonov *et al* 1995) to derive the pre-compensated function I_{pre}. The regularization term is chosen to minimize the second-order derivative of I_{pre} with respect to z. The pre-compensated I function is then calculated as

$$I_{\text{pre}} = \arg\min_{I' \in H} \left(\| I' \otimes k_b - I \|^2 + w \left\| \frac{\mathrm{d}^2}{\mathrm{d}z^2} I'(z) \right\|^2 \right), \tag{17}$$

where $\otimes$ is the convolution operator, w is a weight factor for the regularization and H is the space of continuous, doubly differentiable functions.

The shape of the kernel k_b should be chosen such that it accounts for the average forward-directed scatter. Further insight into this problem can be gained by considering that the initial build-up in the Monte Carlo pencil beams is caused by a similar interface effect but between vacuum and water. Thus, we choose parameters g_1, ν_1 and ν_2 such that I_{pre} does not have any build-up, i.e. is monotonically decreasing. When k_b is applied to the energy distribution, the initial build-up will be reproduced in a manner similar to any subsequent build-up or build-down effects at the heterogeneity interfaces. Optimization methods are used for deriving the free parameters of the kernel.

2.7. Calculation of the energy contribution from extra-focal photons

The energy deposited by the photons originating from the distributed extra-focal photon source is calculated in a way similar to the primary photons. The energy deposited into a grid point p from a pencil-beam beamlet β is determined via (9). However, the depth-directed component $I_\beta(p_z)$ for the primary photons is replaced with a corresponding component $I_{ef}(p_z)$ for the extra-focal photons calculated via (4). The poly-energetic pencil-beam kernel needed in (4) is calculated via (2), where $S_\beta(E)$ has been replaced by the laterally invariant energy spectrum for the extra-focal photons $S_{ef}(E)$. Also, the primary energy fluence Φ_β in (4) needs to be replaced with the extra-focal energy fluence $\Phi_{\beta,ef}(p_z)$, which depends on the depth coordinate p_z. The details on the computation of $\Phi_{\beta,ef}(p_z)$ have been described in Tillikainen *et al* (2007). The change to the divergent coordinate system in (3) is calculated only for the central axis beamlet, and is then applied for all beamlets within the beam area. This process results in $I_{ef}(p_z)$, which does not depend on the lateral position (p_x, p_y) within the beam. The fact that the cylindrical geometry is not exactly valid in the diverging coordinates is ignored for the extra-focal source for simplicity.

The scatter kernels $k_\beta(\theta, \lambda, p_z)$ derived for the primary photons are also used for the extra-focal photons. This is clearly an approximation, since the scatter kernel for the extra-focal photons is different from the primary photon kernal due to lower mean energy. The current approach is used in order to avoid a second fitting of exponential functions to the Monte-Carlo-simulated pencil beams. This approximation does not deteriorate the accuracy significantly, since the contribution from the extra-focal photons is relatively small. The corrections for tissue heterogeneities are performed in the same way as for the primary photons. The same kernel $k_b(d)$ is used for the build-up and build-down corrections as for the primary photons. Effectively, the dose deposition for extra-focal photons is performed along rays that originate from the target. The effects of the distributed source will be taken into account in the energy fluence component $\Phi_{\beta,ef}(p_z)$.

2.8. Calculation of the electron contamination energy contribution

The energy deposited by the contaminating electrons is calculated in the following manner, which is simpler than the approach used for primary and extra-focal photons:

$$E_{\beta,el}(p) = \Phi_{el}(p)c_e(p_z), \tag{18}$$

where $\Phi_{el}(p)$ is the energy fluence of the contaminating electrons and $c_e(p_z)$ is an empirical curve defining the total energy deposited at each plane p_z in a water-equivalent phantom. The energy fluence $\Phi_{\beta,el}(p)$ is calculated as a superposition of two components, both of which are computed as a convolution of the primary energy fluence $\Phi_{prim}(p)$ and a Gaussian (Tillikainen *et al* 2007). The curve $c_e(p_z)$ is determined from the difference between measured and calculated depth–dose curves for the largest field size (Tillikainen *et al* 2007). Hence, the lateral scatter and the build-up and build-down corrections are ignored for the electron

contamination. This can be done for two reasons: (1) the low-energy electrons have a short range in water and (2) the scatter processes are effectively modeled via the energy fluence term $\Phi_{el}(p)$ using the Gaussian convolutions.

2.9. Conversion from energy density to dose

The method presented in previous sections calculates the energy density for each point in the patient geometry. The energy distribution is then converted to dose distribution by dividing the energy density by the relative electron density (ρ_w). This approach produces a better match to Monte Carlo simulations, where the material deduction has been turned off (scaled water approach), than using mass density in the conversion. Hence, the dose to a point r is calculated as

$$D(r) = \frac{E_{b,total}(\mathcal{M}(r))}{\rho_w(r)|\det(J(\mathcal{M}))|}c,\qquad(19)$$

where $E_{b,total}$ is the total energy density computed as a sum of the primary photon, extra-focal photon and electron contamination components, J is the Jacobian of $\mathcal{M}$ evaluated at r and c is a calibration factor, which takes care of the unit conversion from J m^{-3} to Gy MU^{-1}. The calibration factor c is determined based on the measured machine calibration value (Gy MU^{-1}) at a reference geometry and the calculated energy density at the same geometry.

2.10. Test phantoms and beams

To test the developed method, we have calculated dose distributions in the following five test phantoms: (i) a water phantom, (ii) a water phantom with a 10 cm slab of low-density material ($\rho_w = 0.3$) representing lung, (iii) a water phantom with a 5 cm slab of high-density material ($\rho_w = 1.85$) representing bone, (iv) a water phantom with a 10 cm thick block of low-density material placed 2 cm off the CAX, (v) a water phantom with a 5 cm thick block of high-density material placed 2 cm off the CAX. See figures 1(a)–(d) for the dimensions of the test phantoms excluding the simple water phantom. The phantom image sets and treatment plans were created with the Eclipse TPS.

For the water phantom (i), we have compared depth–dose curves for field sizes 30×30, 50×50, 100×100 and 200×200 mm^2 as well as lateral dose profiles at depths 50, 100 and 200 mm for the 200×200 mm^2 field. For the phantoms (ii) and (iii), we have compared depth–dose curves for the same field sizes as for the water phantom. For the phantoms (iv) and (v), we have analyzed lateral dose profiles for a 200×200 mm^2 field at two depths from the phantom surface. Depths of 100 and 160 mm were used for phantom (iv), and 75 and 110 mm for phantom (v). A source-to-phantom distance of 1000 mm was used for all field sizes and phantoms.

The source model used in the calculations was the multiple-source model developed by the authors (Tillikainen *et al* 2007), but since modeling of the primary beam was the main goal of this study, all sources except the primary source were disabled. The primary photon phase space was obtained by configuring the Varian Golden Beam data measurements for 6 and 18 MV beams using the optimization procedure described by the authors (Tillikainen *et al* 2007). The Varian Golden Beam Data is a measurement data set provided by Varian Medical Systems Inc. to be used with commissioning and configuration of Varian Clinac 21EX accelerators. After the source model was constructed, the weights of the electron contamination source and extra-focal source were set to zero, leaving only the primary radiation component.
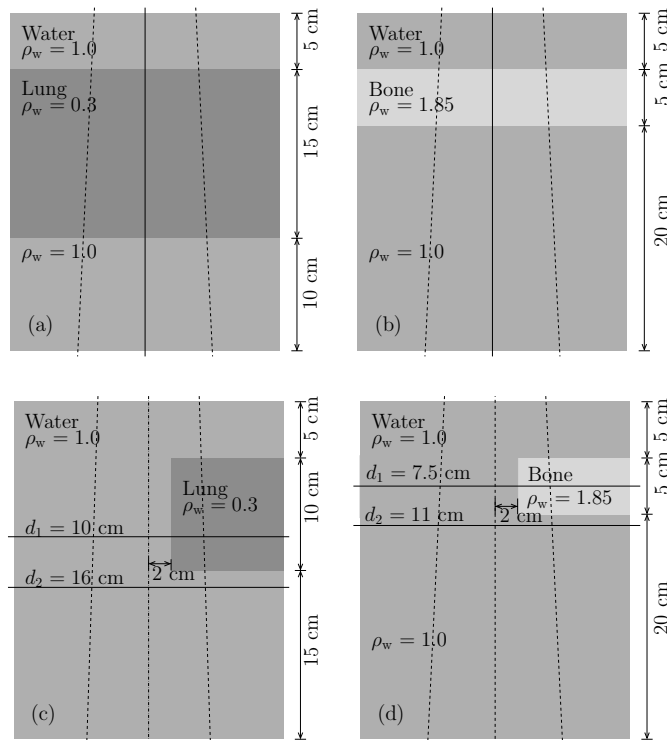
Figure 1. An illustration of four (out of five) test phantoms used in the study: (a) water phantom with a 15 cm lung equivalent slab insert, (b) water phantom with a 5 cm bone equivalent slab insert, (c) water phantom with a 10 cm lung equivalent block insert, 2 cm away from the central axis, and (d) water phantom with a 5 cm bone equivalent block insert, 2 cm away from the central axis. The material names are only suggestive, since the algorithm only uses the relative electron density (ρ_w) information.

2.11. Reference dose calculations using VMC++

The primary aim of the study was to create an algorithm that produces results comparable to Monte Carlo simulations. Hence, the developed method was compared against VMC++ (Kawrakow and Fippel 2000), a fast and accurate Monte Carlo code. The VMC++ plans were run until 0.5% statistical standard uncertainty in the voxels with dose larger than 50% of d_{max} was reached. The dose distribution was not smoothed after the calculation. We used the following parameters for the simulation: grid size = 0.5 cm, ECUT = 0.500 MeV (electron/positron minimum transport energy) and PCUT = 0.05 MeV (photon minimum transport energy). The particle sampling for the VMC++ calculation was performed as described in Tillikainen and Siljamäki (2008) for the primary photon source.

The described 3D pencil-beam superposition algorithm relies on electron densities derived from CT values, and does not have access to the detailed 3D physical structure (material composition) of the phantom or patient. We have therefore chosen to perform the VMC++ calculations with material deduction turned off, using the scaled water approach. As the kernels of the algorithm have also been pre-calculated with Monte Carlo (albeit with the DOSRZnrc user code of EGSnrc), there is a correlation between the calculations of the presented algorithm
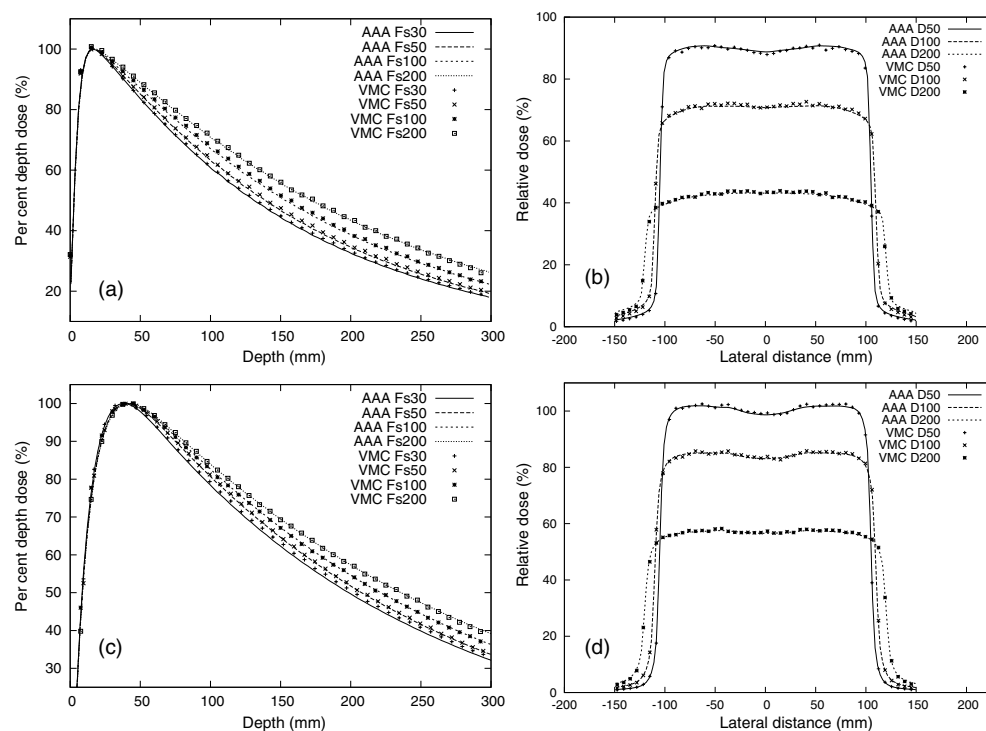
Figure 2. Calculated 'AAA' and MC-simulated 'VMC' depth–dose curves and lateral dose profiles in the water phantom for 6 MV and 18 MV beams. The field size in mm is indicated after letter 'FS' in the figure label and the profile depth in mm after symbol 'D'. (a) Depth–dose curves for 6 MV, (b) profiles for 6 MV, (c) depth–dose curves for 18 MV and (d) profiles for 18 MV.

and VMC++. Because of this, the comparison will primarily point out possible deviations resulting from the approximations and simplifications made within the presented algorithm.

To investigate the effect of the above-mentioned scaling approximation on the VMC++ calculations, a number of fields setups in the lung and bone slab phantoms were re-calculated with material deduction turned on and using the dose-to-medium reporting technique. Dose to medium is expected to correspond better with the true physical dose than dose to water (Siebers *et al* 2000, Liu *et al* 2002). The magnitude of the bias was found to be less than 4% in the cortical bone ($\rho_w = 1.85$) and less than 2% in the lung ($\rho_w = 0.3$) for both the 6 and 18 MV photon beams, respectively.

When comparing the presented algorithm to experimental measurements, apart from possible measurement uncertainties (effective point of measurement, detector noise and positioning), one also has to bear in mind that in most cases, ionization chamber readings are converted to dose to water instead of dose to medium, introducing deviations of the same order of magnitude from the true physical dose as reported above. Another important factor affecting the uncertainty of the patient dose calculation is the accuracy of the source modeling. This issue has been studied extensively in the earlier work by the authors (Tillikainen *et al* 2007). In this work, the same source model was utilized both in the presented algorithm and in VMC++. Despite these uncertainties, the agreement with experimental values has been found to be within clinical acceptance in a large set of cases including solid water and cork phantoms (Fogliata *et al* 2006, Van Esch *et al* 2006, Sterpin *et al* 2007).
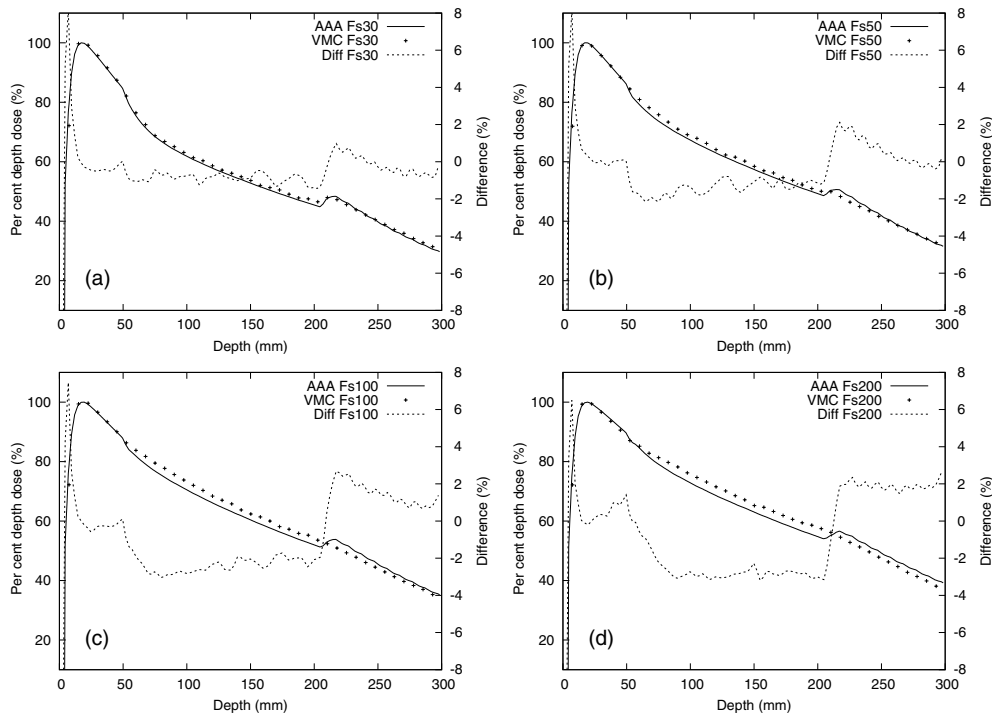
Figure 3. Calculated 'AAA' and MC-simulated 'VMC' depth–dose curves in the lung slab phantom for the 6 MV beam. (a) Field size $30 \times 30\,\text{mm}^2$, (b) $50 \times 50\,\text{mm}^2$, (c) $100 \times 100\,\text{mm}^2$ and (d) $200 \times 200\,\text{mm}^2$.

3. Results

In this section, we compare dose calculations using the presented method with VMC++ Monte Carlo simulations in the test phantoms described in section 2.10. The dose distributions have been normalized to 100% at CAX $d_{\max}$ for each field size.

3.1. Water phantom

The depth–dose curves and lateral dose profiles calculated with the presented method and VMC++ in the water phantom are shown in figures 2(a)–(d) for 6 and 18 MV beams. There is generally a good agreement between the two calculation methods. For 6 MV, the deviations are within (0.5%, 2 mm) for each studied field size. For 18 MV, the deviations are within (0.5%, 2 mm) for the field sizes $50 \times 50, \ldots, 200 \times 200\,\text{mm}^2$, and go up to (1%, 2 mm) for the smallest $30 \times 30\,\text{mm}^2$ field.

3.2. Lung slab phantom

The comparison of depth–dose curves in the lung slab phantom is presented in figures 3(a)–(d) for the 6 MV beam and in figures 4(a)–(d) for the 18 MV beam. For 6 MV, the agreement is best for the $30 \times 30\,\text{mm}^2$ field, where the deviations are in the order of 1% of the field CAX $d_{\max}$. For larger field sizes, the presented method starts to underestimate the dose inside
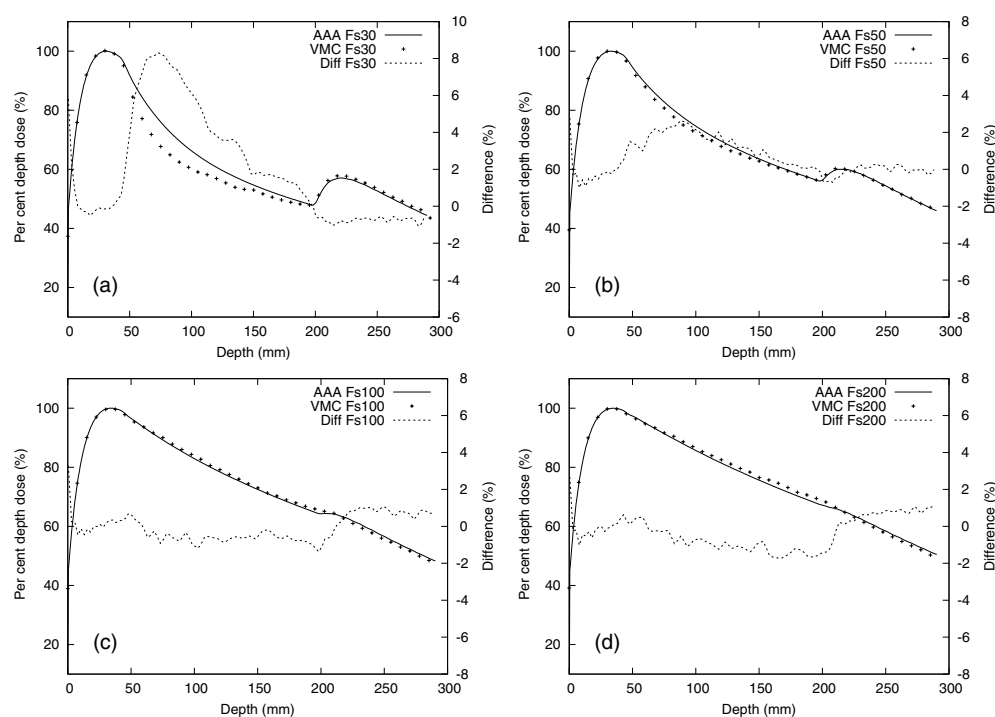
Figure 4. Calculated 'AAA' and MC-simulated 'VMC' depth–dose curves in the lung slab phantom for the 18 MV beam. (a) Field size $30 \times 30 \, \text{mm}^2$, (b) $50 \times 50 \, \text{mm}^2$, (c) $100 \times 100 \, \text{mm}^2$ and (d) $200 \times 200 \, \text{mm}^2$.

the lung and overestimate the dose in the region after the lung insert. The discrepancies are largest for the $200 \times 200 \, \text{mm}^2$ field, where they reach about 3% of field CAX d_{max} within the lung insert and about 2% after the insert. In the region before the lung insert, the deviations are small (within about 1%) for all field sizes. For 18 MV, in contrast to 6 MV, the deviations are largest for the $30 \times 30 \, \text{mm}^2$ field reaching about 8% inside the lung insert. However, for the larger field sizes, the dose underestimation in the lung becomes significantly smaller, and is less severe than for the 6 MV beam. For larger field sizes, the presented method overestimates the dose after the lung insert by about 1%. Again, the dose before the lung slab is well predicted with the presented method.

3.3. Bone slab phantom

The comparison of depth–dose curves in the bone slab phantom is presented in figures 5(a)–(d) for the 6 MV beam and in figures 6(a)–(d) for the 18 MV beam. For 6 MV, the presented method accurately accounts for larger attenuation inside the bone-equivalent material, since the deviations inside the bone insert are in the order of 1% of field CAX d_{max}. However, the interface effects are slightly overestimated for each field size, which results in about 2% deviations near the boundary of the heterogeneity. In the regions before and after the bone insert, the deviations are within 1% for each field size. For 18 MV, the deviations are within about 1% of the field CAX d_{max} for all field sizes in figures 6(a)–(d).
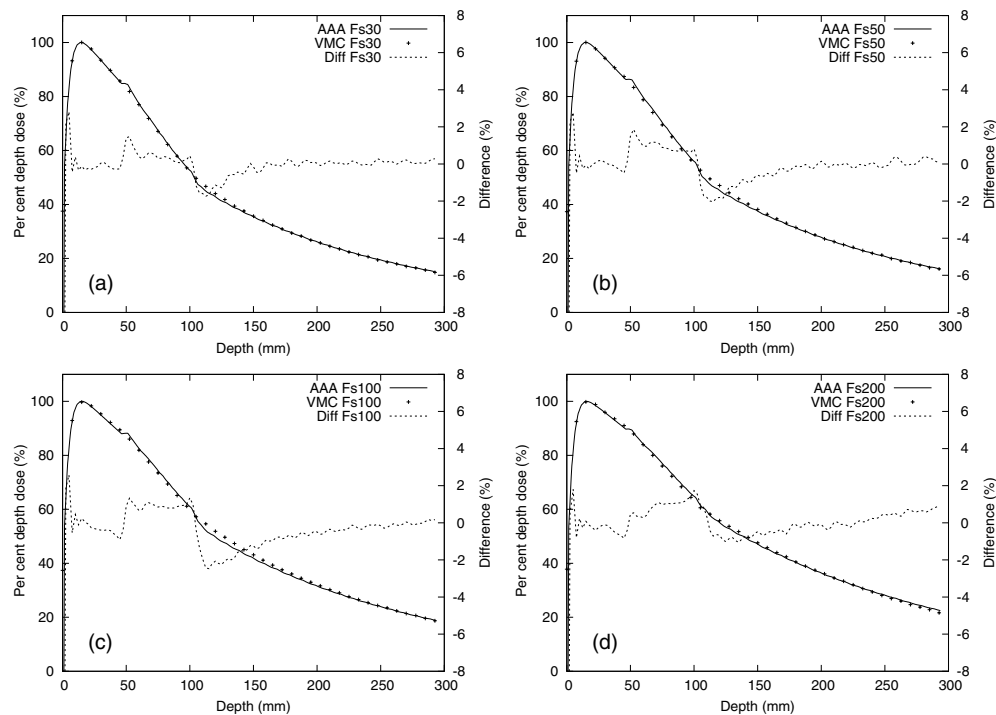
Figure 5. Calculated 'AAA' and MC-simulated 'VMC' depth–dose curves in the bone slab phantom for the 6 MV beam. (a) Field size $30 \times 30 \, \text{mm}^2$, (b) $50 \times 50 \, \text{mm}^2$, (c) $100 \times 100 \, \text{mm}^2$ and (d) $200 \times 200 \, \text{mm}^2$.

3.4. Lung and bone block phantoms

The comparison of the lateral dose profiles at two different depths in the lung block phantom are shown in figures 7(a)–(d) for the 6 and 18 MV beams. The presented method accurately models the lateral material interface for both energies. The largest discrepancies occur for the profile measured at 160 mm for the 6 MV beam in figure 7(b), where an overestimation of about 2% is visible in the region below the lung insert. The results are similar for the bone block phantom shown in figures 8(a)–(d), where the deviations between the methods are mostly within (2%, 2 mm). The largest deviations occur under the bone insert for the 6 MV beam in figure 8(b), where the presented method underestimates the dose by about 2%.

4. Discussion

As presented in section 3, there is generally a good agreement between the calculations utilizing the presented method and Monte Carlo simulations in different kinds of heterogeneous phantoms. Most of the observed discrepancies were within (2%, 2 mm), where the dose difference is specified with respect to the field CAX d_{max}. Considerably larger deviations were found only in the central axis depth dose of the smallest field size ($30 \times 30 \, \text{mm}^2$) in the lung slab phantom for the 18 MV beam. In that case, discrepancies in the order of 8% were observed inside the lung insert ($\rho_{\text{w}} = 0.3$), and considerable discrepancies extended over a few-centimeter region in the low-density material. However, discrepancies of
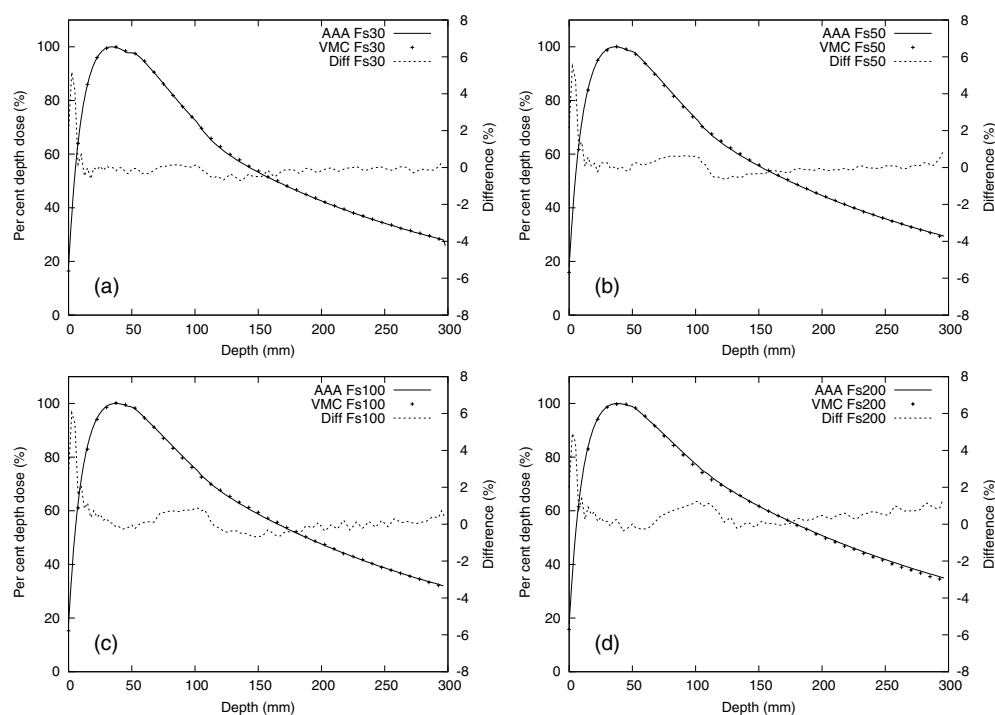
Figure 6. Calculated 'AAA' and MC-simulated 'VMC' depth–dose curves in the bone slab phantom for the 18 MV beam. (a) Field size $30 \times 30 \, \text{mm}^2$, (b) $50 \times 50 \, \text{mm}^2$, (c) $100 \times 100 \, \text{mm}^2$ and (d) $200 \times 200 \, \text{mm}^2$.

comparable magnitude ($\sim 5\%$) have also been reported for the CCC superposition model in similar situations (for a $50 \times 50 \, \text{mm}^2$ field instead of the $30 \times 30 \, \text{mm}^2$ field used in this work) (Arnfield *et al* 2000). In the case of high beam energy and small field size, there is a severe loss of electronic equilibrium on the central axis, which is difficult to model with rectilinear kernel scaling approaches. In reality, the electron and photon scatter does not follow the rectilinear paths assumed in those models. The electronic disequilibrium on the field central axis in the low-density material becomes larger as the field size decreases and the beam energy increases. For small field sizes, there are more electrons traveling away from the corresponding volume element on the central axis than toward it. This is caused by missing scatter from the material outside the geometrical field boundaries, where part of the electrons from the central axis is transported. For the same field size, the electron disequilibrium effect increases as a function of beam energy, since the corresponding electron range increases as well.

The presented method does not tend to underestimate the re-build-up effect on the subsequent lung–water interface like other convolution/superposition models, but the effect is typically overestimated (see e.g. figure 3), especially for larger field sizes. This difference in the algorithm behavior is most likely due to the build-up kernel correction method used in the presented method, which is not used in other superposition/convolution algorithms. The build-up kernel has been designed such that the build-up between vacuum and water is correctly reproduced. However, the build-up effect between lung and water is probably smaller than the effect between vacuum and water due to a smaller density difference, which could explain the observed overestimation in the re-build-up region.
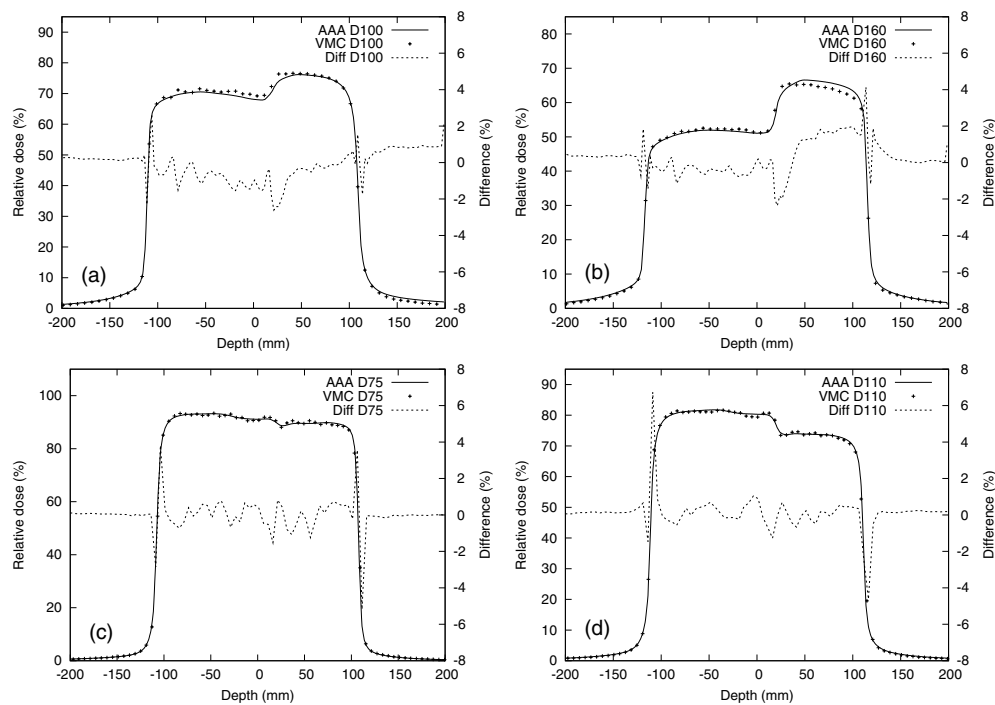
Figure 7. Calculated 'AAA' and MC-simulated 'VMC' dose profiles in the lung block phantom for 6 and 18 MV beams. (a) 6 MV, depth 100 mm; (b) 6 MV, depth 160 mm; (c) 18 MV, depth 100 mm and (d) 18 MV, depth 160 mm.

In the case of the bone-type heterogeneity ($\rho_w = 1.85$), the discrepancies between the presented method and MC simulations are in the order of (2%, 2 mm). For a 6 MV beam, the presented method overestimates the dose systematically about 1% inside the high-density material. For 18 MV in the bone slab phantom, the results are similar than for 6 MV, except that the discrepancies near the border of the heterogeneity are smaller. However, when compared to true physical doses, the bias (up to 4%) caused by the scaling approach used in VMC++ calculations should be taken into account. As demonstrated in figures 7 and 8, the developed method models lateral heterogeneities (both water–lung and water–bone interfaces) with excellent accuracy. The scaling process applied to the lateral scatter kernels is important for obtaining good accuracy in these cases.

When compared to previously published experimental verification of the presented method (Van Esch *et al* 2006), some agreements and some disagreements were found. In the work of Van Esch *et al* (2006), the current method was compared to the ionization chamber and film measurements in several homogeneous and heterogeneous phantoms. The lateral profile comparisons in the phantom with the cork insert are in good agreement with the results in the lung block phantom shown in figure 7. Also the depth–dose comparisons in the lung slab phantom for 18 MV in figure 4 are consistent with the earlier findings, if the normalization to the field CAX d_{max} used in this work is taken into account in the comparison. However, the corresponding depth–dose comparisons for 6 MV show a significantly better agreement with the MC simulations in this work than the comparisons to ionization chamber measurements presented by Van Esch *et al* (2006). This apparent contradiction can be explained by the fact that the ionization chamber itself can cause significant dose perturbations (6, ..., 12%) at the
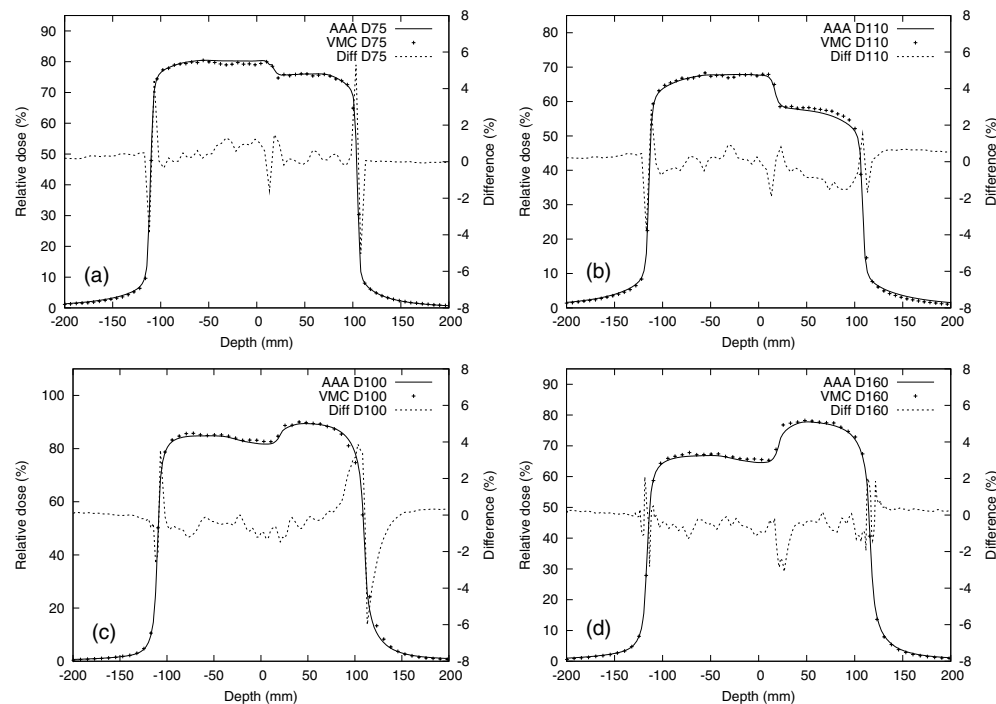
Figure 8. Calculated 'AAA' and MC-simulated 'VMC' dose profiles in the bone block phantom for 6 and 18 MV beams. (a) 6 MV, depth 75 mm; (b) 6 MV, depth 110 mm; (c) 18 MV, depth 75 mm and (d) 18 MV, depth 110 mm.

point of measurement in the case of electronic disequilibrium (Ding *et al* 2007). These kinds of perturbations occur especially for a small field size in low-density media.

If an even better calculation accuracy in heterogeneous geometries is required, a method based on first principles—rather than macroscopic characterizations—should be applied. However, these methods have their own challenges when applied to clinical planning, including the modeling of the phase space, computation time and statistical noise (in the case of Monte Carlo). The calculation time of the presented method could be further improved in the future by adopting a multi-resolution approach, i.e. by performing the lateral scatter operation on a subsampled electron density image for components of a different range ($1/\mu_i$) and combining the results at the end. The fitting of the exponential functions to the MC data in (7) and (8) is currently performed on-line during the dose calculation. Hence, further speed-up could possibly be achieved by pre-calculating the coefficients $c_i(\theta, p_z)$ in (6), since they are independent of the patient data. However, the coefficients would have to be calculated for each exponential component, angular sector, radiological depth and beamlet, which would result in a database with a size of ~50 MB, depending on the selected grid spacing for the beamlets and the radiological depth.

5. Conclusions

In this work, a three-dimensional pencil-beam kernel superposition method for photon dose calculation was presented. The developed method is conceptually simple, and results in accurate dose distributions in a wide range of conditions. The largest limitations were detected

in a lung-equivalent slab phantom in the case of a small field size and large beam energy. This should be recognized as a limitation of the presented method. However, large photon energies ($\geqslant 15$ MV) should normally not be used for conformal lung cancer treatments due to inferior target coverage compared to smaller photon energies (Wang *et al* 2002). The bias caused by the scaling approximation to the Monte Carlo simulation (up to 4% in cortical bone) should be taken into account when comparing the presented calculation results to true physical doses.

The running time of the computer implementation of the method is about 10 s for a $40 \times 40\,\text{mm}^2$ field and about 60 s for a $400 \times 400\,\text{mm}^2$ field (on a dual-core Intel Xeon 5160 platform with 8 GB of memory and two processors). This makes the presented algorithm suitable for routine clinical planning even if multiple re-calculations are needed.

Acknowledgments

References

Ahnesjö A and Aspradakis M M 1999 Dose calculations for external photon beams in radiotherapy *Phys. Med. Biol.* **44** R99–R155
Arnfield M R, Hartmann Sintar C, Siebers J, Garmon P, Cox L and Mohan R 2000 The impact of electron transport on the accuracy of computed dose *Med. Phys.* **27** 1266–74
Boyer A L and Mok E C 1986 Calculation of photon dose distributions in an inhomogeneous medium using convolutions *Med. Phys.* **13** 503–9
Cassell K J, Hobday P A and Parker R P 1981 The implementation of a generalised Batho inhomogeneity correction for radiotherapy planning with direct use of CT numbers *Phys. Med. Biol.* **26** 825–33
Ding G X, Duggan D M and Coffey C W 2007 Comment on 'Testing of the analytical anisotropic algorithm for photon dose calculation [Med. Phys. 33, 4130-4148 (2006)] *Med. Phys.* **34** 3414
Fogliata A, Nicolini G, Vanetti E, Clivio A and Cozzi L 2006 Dosimetric validation of the anisotropic analytical algorithm for photon dose calculation: fundamental characterization in water *Phys. Med. Biol.* **51** 1421–38
Gifford K A, Horton J L Jr, Wareing T A, Failla G and Mourtada F 2006 Comparison of a finite-element multigroup discrete-ordinates code with Monte Carlo for radiotherapy calculations *Phys. Med. Biol.* **51** 2253–65
Kawrakow I 2000 Accurate condensed history Monte Carlo simulation of electron transport I EGSnrc, the new EGS4 version *Med. Phys.* **27** 485–98
Kawrakow I and Fippel M 2000 VMC++, a fast MC algorithm for Radiation Treatment planning *Proc. 13th Int. Conf. on the Use of Computers in Radiation Therapy (ICCR)* (Heidelberg: Springer Verlag) pp 126–8
Liu H H, Keall P and (Moderator) Hendee W R 2002 Dm rather than dw should be used in Monte Carlo treatment planning *Med. Phys.* **29** 922–4
Ma C-M, Mok E, Kapur A, Pawlicki T, Findley D, Brain S, Forster K and Boyer A L 1999 Clinical implementation of a Monte Carlo treatment planning system *Med. Phys.* **26** 2133–43
Mackie T R, Scrimger J W and Battista J J 1985 A convolution method of calculating dose for 15-MV x rays *Med. Phys.* **12** 188–96
Miften M, Wiesmeyer M, Monthofer S and Krippner K 2000 Implementation of FFT convolution and multigrid superposition models in the FOCUS RTP system *Phys. Med. Biol.* **45** 817–33
Neuenschwander H, Mackie T R and Reckwerdt P J 1995 MMC—a high-performance Monte Carlo code for electron beam treatment planning *Phys. Med. Biol.* **40** 543–74
Seco J and Evans P M 2006 Assessing the effect of electron density in photon dose calculations *Med. Phys.* **33** 540–52
Sharpe M B and Battista J J 1993 Dose calculations using convolution and superposition principles: the orientation of dose spread kernels in divergent x-ray beams *Med. Phys.* **20** 1685–94
Siebers J V, Keall P J, Nahum A E and Mohan R 2000 Converting absorbed dose to medium to absorbed dose to water for Monte Carlo based photon beam dose calculations *Phys. Med. Biol.* **45** 983–95
Sontag M R and Cunningham J R 1977 Corrections to absorbed dose calculations for tissue inhomogeneities *Med. Phys.* **4** 431–6

Sterpin E, Tomsej M, De Smedt B, Reynaert N and Vynckier S 2007 Monte Carlo evaluation of the AAA treatment planning algorithm in heterogeneous multilayer phantom and IMRT clinical treatments for an Elekta SL25 linear accelerator *Med. Phys.* **34** 1665–77

Storchi P R M, van Battum L J and Woudstra E 1999 Calculation of a pencil beam kernel from measured photon beam data *Phys. Med. Biol.* **44** 2917–28

Tikhonov A N, Goncharsky A, Stepanov V V and Yagola A G 1995 *Numerical Methods for the Solution of Ill-Posed Problems* (Berlin: Springer)

Tillikainen L and Siljamäki S 2008 A multiple-source photon beam model and its commissioning process for VMC++ Monte Carlo code *J. Phys.: Conf. Ser.* **102** 012024

Tillikainen L, Siljamäki S, Helminen H, Alakuijala J and Pyyry J 2007 Determination of parameters for a multiple-source model of megavoltage photon beams using optimization methods *Phys. Med. Biol.* **52** 1441–67

Ulmer W, Pyyry J and Kaissl W 2005 A 3D photon superposition/convolution algorithm and its foundation on results of Monte Carlo calculations *Phys. Med. Biol.* **50** 1767–90

Van Esch A, Tillikainen L, Pyykkönen J, Tenhunen M, Helminen H, Siljamäki S, Alakuijala J, Paiusco M, Iori M and Huyskens D P 2006 Testing of the analytical anisotropic algorithm for photon dose calculation *Med. Phys.* **33** 4130–48

Wang L, Yorke E, Desobry G and Chui C-S 2002 Dosimetric advantage of using 6 MV over 15 MV photons in conformal therapy of lung cancer: Monte Carlo studies in patient geometries *J. Appl. Clin. Med. Phys.* **3** 51–9

Wareing T, Vassiliev O, Failla G, Davis I, McGhee J, Barnett D, Horton J and Mourtada F 2007 TU-EE-A1-01: validation of a prototype deterministic solver for photon beam dose calculations on acquired CT data in the presence of narrow beams and heterogeneities *Med. Phys.* **34** 2565